Rare Metal Materials and Engineering
Volume 52, Issue 3, March 2023
Available online at www.rmme.ac.cn

Science Press

Cite this article as: Yin Hongliang, Meng Lingjian, Lu Yupeng, et al. Experiment and Numerical Simulation of Ti-22Al-25Nb Alloy Sheet by Gas Bulging[J]. Rare Metal Materials and Engineering, 2023, 52(03): 806-814.

ARTICLE

Experiment and Numerical Simulation of Ti-22Al-25Nb Alloy Sheet by Gas Bulging

Yin Hongliang[1], Meng Lingjian[1], Lu Yupeng[1], Lin Peng[1,2]

[1] College of Materials Science and Engineering, Taiyuan University of Technology, Taiyuan 030024, China; [2] National Key Laboratory of Science and Technology on Precision Heat Processing of Metals, Harbin Institute of Technology, Harbin 150001, China

Abstract: The hot formability of Ti-22Al-25Nb alloy sheet at elevated temperatures was studied through the gas bulging experiments and numerical simulation. The distributions of bulging shell shape and wall thickness at 930 and 970 °C were analyzed. The microstructure and mechanical properties of the bulging part were discussed. Results show that the bulging shell is close to the spherical surface in the initial bulging stage, and it gradually becomes ellipsoid with increasing the bulging height. At 930 and 970 °C, the final bulging height reaches 46.25 and 49.85 mm, and the curvature radius of shell top reaches 49.33 and 49.19 mm, respectively. The wall thickness of bulging part is inhomogeneous: it gradually decreases from the bottom region to the top region. The deformation temperature strongly affects the shape of bulging part: the partial bulging shape is more inhomogeneous at low temperature of 930 °C. Under the same bulging height, the curvature radius of bulging is lower and the thinning ratio is higher at 930 °C. In addition, the O phase is precipitated and spheroidized during bulging at 930 °C, which causes the generation of O type and V type cavities and the reduction in microhardness. However, the microstructure is uniformly distributed after bulging at 970 °C. O phase is precipitated during the cooling process in lamellar morphology, which strengthens the bulging part.

Key words: Ti_2AlNb; gas bulging; hot formability; microstructure

Ti_2AlNb-based alloys are regarded as one of the most potential aircraft structure materials to serve at 600–750 °C due to their superior properties, such as high strength, low density, and high creep/oxidation resistance[1–4]. Banerjee et al[5] reported the orthorhombic Ti_2AlNb phase with the *Cmcm* space group. Since then, the Ti_2AlNb-based alloys have been widely researched for industrial application[3,6–9].

Ti_2AlNb-based alloys may exhibit O, α_2, and β_2 phases, therefore leading to various microstructures and different mechanical properties. Gogia et al[10] reviewed the relationship between the microstructure and mechanical properties of Ti-Al-Nb alloys. The amount and distribution of B2 phase and the scale of O laths both influence the tensile properties of alloys, while the creep properties are determined by the volume fraction and morphology of equiaxed O phase. Germann et al[11] studied the effect of chemical composition on microstructure and mechanical properties of Ti-22Al-25Nb alloy. It is reported that the alloy with high Al/Nb ratio shows the high oxidation resistance and low ductility due to the multiphase microstructures. Jia et al[12] studied the microstructure and mechanical properties of hot-pressed Ti-22Al-25Nb alloy at 950–1200 °C, and found that with increasing the hot pressing temperature, the alloy ductility is increased due to the increase in B2 grain size and lamellar O phase content. Lin et al[13] reported the tensile deformation behavior of Ti-22Al-25Nb alloy at 930–990 °C, and clarified that the work hardening and strain rate hardening are the hardening mechanisms in this tensile deformation process, whereas the dynamic recovery is the softening mechanism. These extensive researches on Ti_2AlNb-based alloys provide the fundamental guidance and promote the application progress.

However, the Ti_2AlNb-based alloys exhibit poor ductility, large springback, and restricted formability at room temperature due to their intrinsic brittleness, which severely hinders the formation of components with complex shape. Therefore, the Ti_2AlNb-based alloys are usually processed at high temperatures of 900 – 1000 °C by various forming processes. Hot gas bulging technique is one of the promising

Received date: August 08, 2022
Foundation item: National Natural Science Foundation of China (51505323); Applied Basic Research Program of Shanxi Province (20210302123117, 20210302124658)
Corresponding author: Lin Peng, Ph. D., Professor, College of Materials Science and Engineering, Taiyuan University of Technology, Taiyuan 030024, P. R. China, Tel: 0086-351-6010021, E-mail: linpeng@tyut.edu.cn

methods for the formation of low ductility metals, such as high strength steels, titanium alloys, and magnesium alloys[14–16]. The low deformation resistance, high formability, and high forming efficiency of hot gas bulging technique all promote the efficient formation of sheet or tube components with complex shape[17]. Therefore, the deformation mechanism and formability of Ti_2AlNb-based alloys after hot gas bulging have been researched. Wu et al[18] investigated the microstructure and formability of rolled Ti22Al24.5Nb0.5Mo alloy sheet after hot gas bulging at 970 °C. The predicted forming limit curve by Logan-Hosford function fits well with the experiment data. The main deformation mechanism in tension-tension bulging tests is dynamic recrystallization. Kong et al[19] reported the microstructure and texture evolution during hot gas free bulging process of the laser-welded Ti-22Al-25Nb alloy tube, and clarified that the dynamic recovery in β/B2 phase is the dominant mechanism rather than the dynamic recrystallization with increasing the temperature from 950 °C to 980 °C. The mechanical properties of the Ti_2AlNb-based alloys after hot gas bulging have also been investigated. Wu et al[20] studied the microstructure and mechanical properties of hot-gas formed Ti_2AlNb parts. The alloy strength is decreased with decreasing the forming temperature (930 and 950 °C) and increasing the strain rate (0.1 and 0.01 s^{-1}). Because the dynamic recovery is slower than the dislocation generation, the alloy strength is decreased, resulting in the damage of dislocations. Jiao et al[21] investigated the effect of in-die cooling parameters on microstructure and mechanical properties of hot-gas formed Ti-22Al-24Nb-0.5Mo quadrate tubes. The volume fraction of O platelets is increased with decreasing the cooling airflow pressure, which increases the tensile strength.

Although abundant fundamental researches have been made on Ti_2AlNb-based alloys, the hot formability of Ti-22Al-25Nb alloy sheet after hot gas bulging process at various uniform temperatures is rarely reported. Since the temperature strongly affects the deformation behavior, microstructure, and mechanical properties of Ti-22Al-25Nb alloy[13], it is of importance to study the effect of bulging temperature on the sheet formability. Therefore, this research investigated the hot formability of Ti-22Al-25Nb alloy sheet after hot gas bulging, providing guidance for the bulging parameter design in industrial production. In addition, the gas bulging tests were conducted at high temperatures of 930 and 970 °C. The microstructure, geometric shape, mechanical properties, and distribution of bulging parts were analyzed. Meanwhile, the numerical simulation of hot formability of Ti-22Al-25Nb alloy was predicted by the finite element method (FEM), and the simulation results were compared with the experiment data to evaluate the prediction accuracy.

1 Experiment

The hot rolled Ti-22Al-25Nb (at%) sheet (Central Iron and Steel Research Institute, Beijing, China) with the thickness of 1.3±0.5 mm was used as raw material. The as-received sheet was heated at 1000 °C for 2 h. Then, the sheet was cut into specimens of 165 mm×165 mm×1.33 mm along the rolling direction (RD), transverse direction (TD), and normal direction (ND).

The hot gas bulging process was conducted through the specific equipment, which consisted of forging machine, furnace, and the bulging dies, as shown in Fig.1. The bulging dies with the inside diameter of 110 mm and the radius of 3 mm were manufactured from the 3Cr24Ni7SiNRE nickel-alloy. Two holes were separately designed on the clamp plate and die as the entrance and the outlet for argon gas. The Ti-22Al-25Nb alloy sheet was placed between the die and clamp plate before bulging experiment. Then, the assembled parts were heated in the furnace until the bulging temperature. It is known that the microstructure and phase composition of Ti-22Al-25Nb alloy are highly influenced by the forming temperature. Thus, the bulging temperatures in this research were designed as 930 (B2+O dual-phase region) and 970 °C (α_2+B2+O triple-phase region) to analyze the effect of microstructure on the bulging formability. During the bulging tests, the sealing requirement was satisfied by the pressing of 100 kN forging machine. The flowing of materials from the flange area to the bulging area could also be prevented. The real-time temperature of the sheets and dies was measured by the K-type thermocouple. The argon gas blew into the dies through the small gas intake on the clamp plat. Fig.2 shows the loading paths of gas bulging pressure at 930 and 970 °C. The bulging pressure increased gradually to 3.5 MPa at 930 °C and to 1.5 MPa at 970 °C. Then, the pressure was kept constant in the subsequent bulging process. The bulging parts were furnace-cooled to room temperature after bulging process.

The as-received alloy sheet and the bulging parts were cut

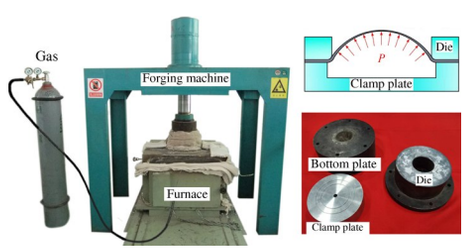

Fig.1 Equipment for high temperature gas forming

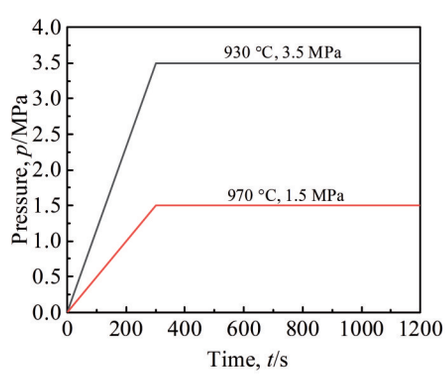

Fig.2 Schematic diagram of loading paths of gas bulging pressure at 930 and 970 °C

and metallographically polished. Then, they were electro-polished at 45 V and − 40 °C with the solution of 6vol% perchloric acid, 34vol% butarol, and 60vol% carbinol. The microstructure was analyzed by scanning electron microscope (SEM, FEI Quanta 200 FEG) coupled with electron backscatter diffractometer (EBSD). The ND-RD plane of as-received alloy sheet and the vertical section of bulging parts were analyzed. EBSD observation was conducted with a step size of 1.0 mm and then analyzed by TSL Orientation Imaging Microscopy Analysis V5.31 software. Furthermore, X-ray diffraction (XRD, Shimadzu XRD-6000) analysis was conducted with Cu Kα radiation source at acceleration voltage of 40 kV. The specimens were characterized by transmission electron microscope (TEM, FEI Tecnai G^2 F30) to identify the phase composition. The selected area electron diffraction (SAED) patterns were analyzed by the Gatan Digital Micrograph 3.0 and MDI Jade 5.0 software. The mechanical properties of the bulging parts were investigated through the microhardness tests by HVS-1000A microhardness tester.

2 Numerical Simulation

Table 1 Material parameters for numerical simulation at 970 °C and strain rate of 1.0×10^{-3} s^{-1} [13]

Mass density/ g·cm^{-3}	Young's modulus/MPa	Poisson's ratio	K	n	m
5.3	322 400	0.4	585.81	0	0.2956

The numerical simulation of hot gas bulging process was performed by FEM-based software DYNAFORM V5.6 with the LS-DYNA solver. The distribution of wall thickness and the geometry shape change after bulging were investigated through the numerical simulation. Fig. 3 shows FEM model and the meshing for gas bulging. The inside diameter/radius of die and the sheet size were the same as the experiment parameters. The sheet mesh size was 3.0 mm. The maximum and minimum mesh size of die were 30 and 0.5 mm, respectively. The material parameters of Ti-22Al-25Nb alloy sheet were obtained by hot tensile tests at 930 and 970 °C and strain rate of 1.0×10^{-3} s^{-1}, as reported in Ref. [13]. Table 1 summarizes the material parameters used for the simulation at 970 ° C and strain rate of 1.0×10^{-3} s^{-1}. The Backoften constitutive equations at 930 and 970 °C can be expressed by Eq.(1) and Eq.(2), respectively, as follows:

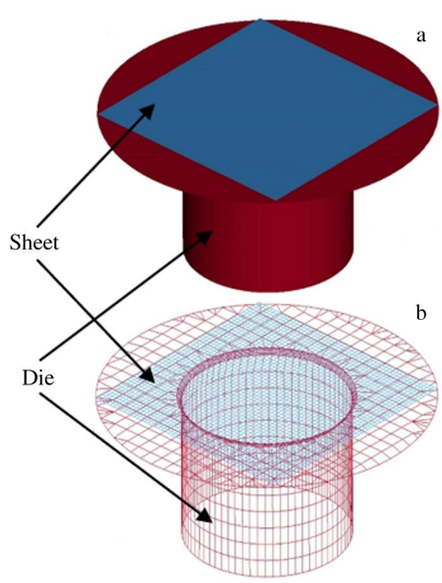

Fig.3 Schematic diagrams of FEM model (a) and meshing for sheet formation (b)

$$\sigma = 875.38\dot{\varepsilon}^{0.24} \tag{1}$$

$$\sigma = 581.58\dot{\varepsilon}^{0.30} \tag{2}$$

where σ is the stress and $\dot{\varepsilon}$ is the strain rate. The simulation was based on the superplastic forming model[22–23]. Song et al[22] established the geometric equations, mechanical equilibrium equation, and constitutive equation to obtain the stress and strain rate distribution of free bulging process. Hill et al[23] proposed the Rosserd viscoplastic constitutive equation and increment theory, as follows:

$$\sigma = K\varepsilon^n\dot{\varepsilon}^m \tag{3}$$

$$\frac{\dot{\varepsilon}_\mathrm{r}}{\sigma_\mathrm{r}-\left[\frac{R}{(1+R)}\right]\sigma_\theta} = \frac{\dot{\varepsilon}_\theta}{\sigma_\theta-\left[\frac{R}{(1+R)}\right]\sigma_\mathrm{r}} = \frac{\dot{\varepsilon}_\mathrm{e}}{\sigma_\mathrm{e}} \tag{4}$$

where K is the material constant; n is the hardening index; m is the strain rate sensitivity index; ε is the strain; σ_e, $\dot{\varepsilon}_\mathrm{e}$, and R are equivalent stress, equivalent strain rate, and the ratio of width to thickness, respectively; σ_r and $\dot{\varepsilon}_\mathrm{r}$ are the stress and strain rate along RD, respectively; σ_θ and $\dot{\varepsilon}_\theta$ are the stress and strain rate along TD, respectively. The values of σ_e and $\dot{\varepsilon}_\mathrm{e}$ can be calculated by Eq.(5) and Eq.(6), respectively:

$$\sigma_\mathrm{e} = \left[\sigma_\mathrm{r}^2+\sigma_\theta^2-\frac{2R}{1+R}\sigma_\mathrm{r}\sigma_\theta\right]^{\frac{1}{2}} \tag{5}$$

$$\dot{\varepsilon}_\mathrm{e} = \frac{1+R}{(1+2R)^{\frac{1}{2}}}\left[\dot{\varepsilon}_\mathrm{r}^2+\dot{\varepsilon}_\theta^2-\frac{2R}{1+R}\dot{\varepsilon}_\mathrm{r}\dot{\varepsilon}_\theta\right]^{\frac{1}{2}} \tag{6}$$

Then, the final equations can be obtained, as follows:

$$\begin{cases} \varepsilon_\mathrm{r} = \varepsilon_\theta = -\dfrac{1}{2}\varepsilon_\mathrm{S} = \ln(1+hy) \\ S = \dfrac{s_0}{(1+hy)^2} \\ \sigma_\mathrm{r} = \sigma_\theta = \dfrac{pr_\mathrm{c}}{4s_0}\dfrac{1+h^2}{h}(1+hy) \\ \dot{\varepsilon}_\mathrm{r} = \dot{\varepsilon}_\theta = -\dfrac{1}{2}\dot{\varepsilon}_\mathrm{S} = \dfrac{2y}{1+h^2}\dfrac{\mathrm{d}h}{\mathrm{d}t} \end{cases} \tag{7}$$

where ε_r, ε_θ, and ε_s are the strain along RD, TD, and ND, respectively; $\dot{\varepsilon}_\mathrm{S}$ is strain rate along ND; t is bulging time; r_c is the diameter of die inner hole; h and y are related parameters; s is the instantaneous thickness during bulging; s_0 is the original thickness of sheet; p is bulging pressure. h and y can be calculated by Eq.(8) and Eq.(9), respectively:

$$h = \frac{h_\mathrm{d}}{r_\mathrm{c}} \tag{8}$$

$$y = \frac{\omega}{r_\mathrm{c}} \tag{9}$$

where h_d is bulge height; ω is the distance from point M (Fig.4) to the bottom of expanded part. The related parameters of sheet free bulging and their lengths are shown in Fig.4.

3 Results and Discussion

3.1 Microstructure and phase components of as-received alloy sheet

Fig. 5 shows the microstructures and phase components of the as-received alloy sheet after heat treatment. A tri-modal microstructure composed of equiaxed α_2 phase, lamella O phase, and B2 matrix can be observed by SEM at backscattered-electron (BSE) mode, as shown in Fig. 5a. The black equiaxed α_2 phase with low Nb content is distributed homogeneously in the B2 matrix, indicating that the α_2 phase is adequately spheroidized during hot rolling process. A little lamellar O phase is precipitated at the grain boundaries and inside the B2 grains during the cooling process from annealing temperature to room temperature. The grain orientation distribution of the α_2 and B2 phases is shown in Fig.5b. B2 phase shows a strong basal texture and the α_2 phase shows a transverse texture, which are typical hot rolling textures in body-centered cubic and hexagonal close packed metals[24–25]. This result indicates that the rolling texture remains in the alloy sheet even after the heat treatment for 2 h. According to XRD pattern in Fig. 5c, the α_2 phase, O phase, and B2 phase can be identified, which agrees well with the above microstructure analysis. TEM analysis was performed to further confirm the phase composition, as shown in Fig. 6. The dark and bright areas in Fig.6a represent B2 phase and α_2 phase, which are further identified through SAED patterns in Fig.6b and 6c, respectively.

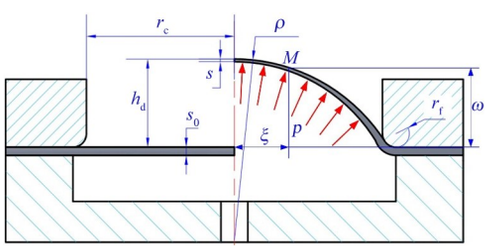

Fig.4 Schematic diagram of sheet free bulging

3.2 Geometrical shape change during bulging process

If the alloy sheet belongs to a part of spherical surface during bulging, the theoretical relationship between the bulging height h_d and top region curvature radius ρ can be satisfied, as follows:

$$\rho = \frac{r_c^2 + h_d^2}{2h_d} \tag{10}$$

$$\rho = \frac{(r_c + r_f)^2 + h_d^2 - 2r_f h_d}{2h_d} \tag{11}$$

where r_f is the die corner radius. Eq. (10) describes the relationship without consideration of the die corner radius, and Eq. (11) describes the relationship with consideration of die corner radius. The theoretical relationship curves between bulging height h and curvature radius ρ are shown in Fig. 7. The experiment results of bulging at 930 and 970 °C are also

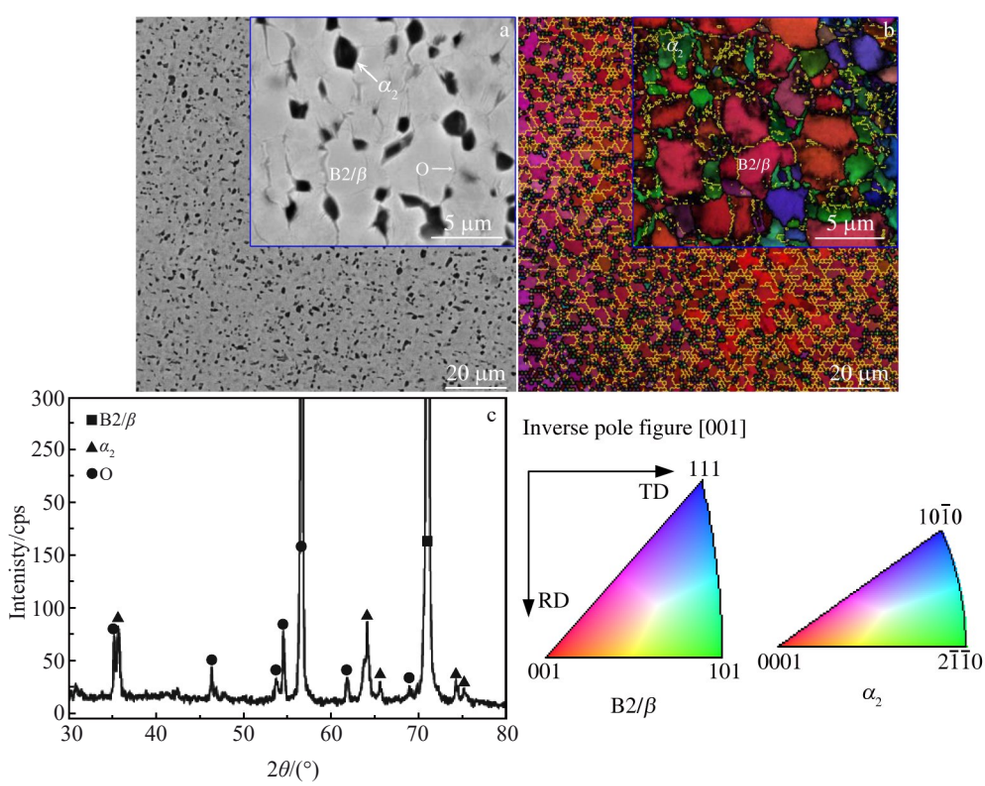

Fig.5 SEM-BSE microstructure (a), grain orientation distribution (b), and XRD pattern (c) of as-received alloy sheet after heat treatment

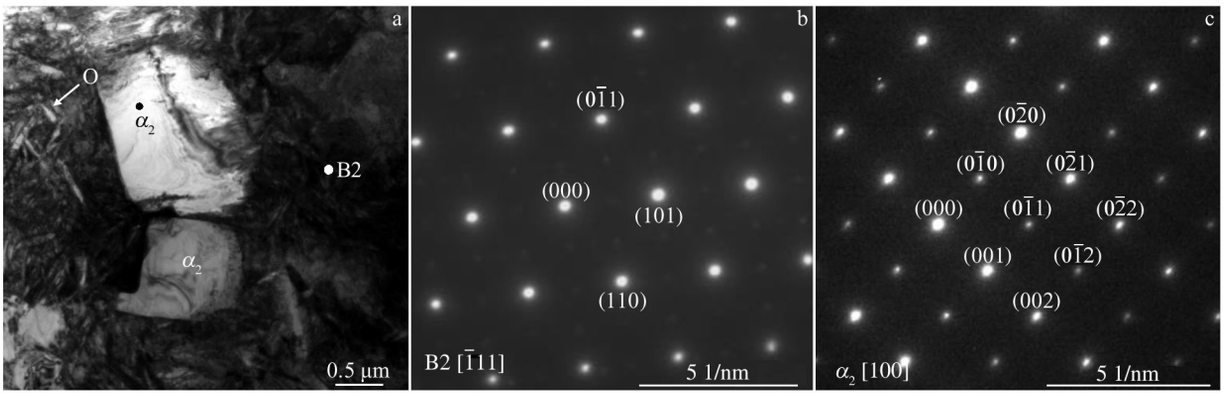

Fig.6 TEM microstructure of as-received alloy sheet (a); SAED patterns of the marked B2 phase (b) and α_2 phase (c) in Fig.6a

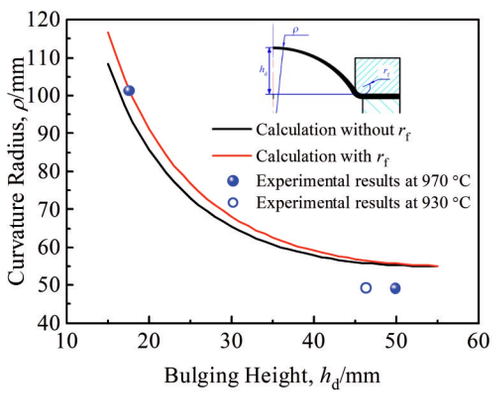

Fig.7 Simulated and experimental results of curvature radius ρ with bulging height h_d

shown in Fig.7 for comparison. The curvature radii calculated with and without consideration of r_f are both decreased with increasing the bulging height. However, the calculated curvature radius with consideration of corner radius is higher than that without consideration of corner radius, and the difference between these two values is decreased with increasing the bulging height. This phenomenon indicates that the effect of corner radius on the calculated curvature radius is weakened with the bulging process proceeding.

The geometrical shape change was also investigated through the practical bulging parts. The bulging pressure is gradually increased from 0.0 MPa to 1.5 MPa and then kept constant at 970 °C for bulging. Fig.8 shows the bulging part after increasing the pressure from 0.0 to 1.5 MPa at 970 °C. The bulging height reaches 17.5 mm and the curvature radius on the shell top reaches 101.35 mm. This result suggests that the shell is already deformed before the pressure reaches 1.5 MPa. In addition, the curvature radius of the bulging part is almost equal to that of the calculated value, as shown in Fig.7, which denotes that the shell is close to the part of spherical surface during the pressure increasing stage. Fig.9 shows the final bulging parts after bulging process at constant pressure of 1.5 MPa and temperature of 970 °C and at 3.5 MPa and 930 °C. The bulging height reaches 46.25 and 49.85 mm and the curvature radius on the shell top reaches 49.33 and 49.19 mm at 930 and 970 °C, respectively. The bulging height at 930 °C is lower than that at 970 °C, whereas the curvature radii are similar to each other. The experimental bulging height and curvature radius are both lower than the theoretical ones, which illustrates that the bulging shape gradually deviates from the ideal spherical shell during the bulging process. The bulge heights are different at 930 and 970 °C. Thus, it can be predicted that the low bulging temperature causes the low curvature radius under the same bulging height condition.

The numerical simulation results of bulging at 930 and 970 °C are shown in Fig.10. The bulging height is set as 49.85 mm. The curvature radius on the shell top reaches 50.42 and 55.06 mm at 930 and 970 °C, respectively, which confirms the prediction that the low bulging temperature causes the low curvature radius under the same bulging height condition. This result may be explained by different deformation behavior of Ti-22Al-25Nb alloy at different temperatures. It is known that the bulging deformation at high temperatures is inhomogeneous: the stain rate and strain are high at the top region and low at the bottom region. The deformation uniformity is strongly affected by the strain hardening and strain rate hardening effects[26–27]. The deformation mechanism and strain rate sensitivity (m) of Ti-22Al-25Nb alloy at 930 and 970 °C are discussed in Ref. [13]. The strain hardening effect is restricted above 900 °C and the m value is increased with increasing the temperature. These results all illustrate

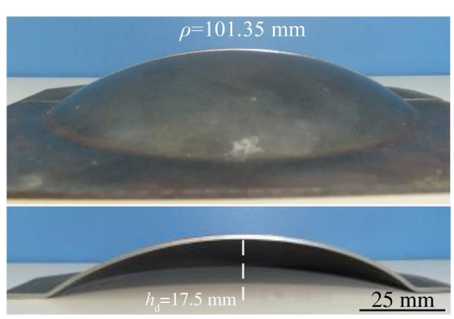

Fig.8 Appearances of bulging part with increasing the pressure from 0.0 MPa to 1.5 MPa at 970 °C

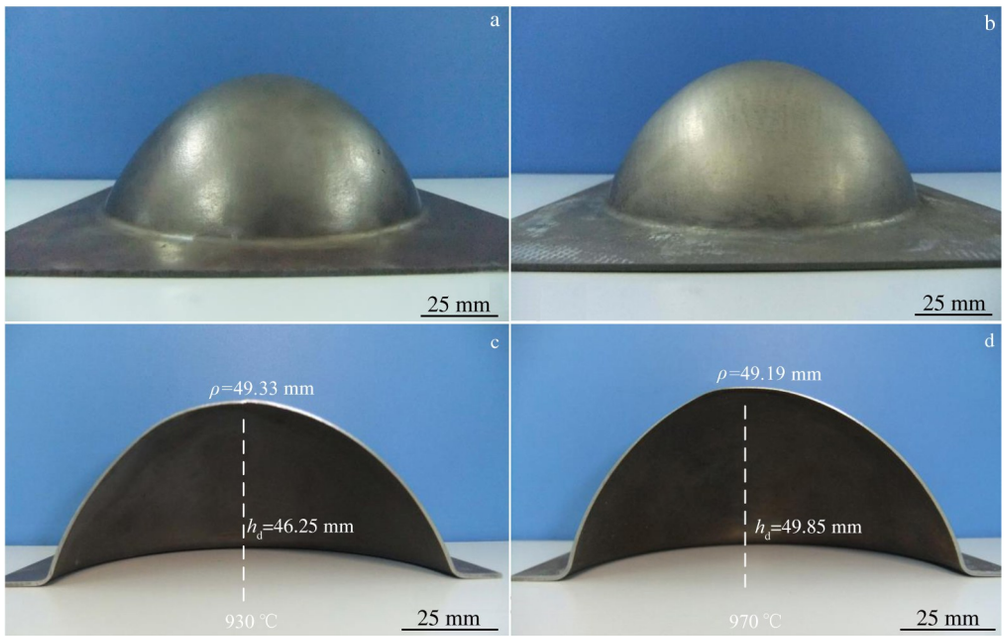

Fig.9 Appearances of final bulging parts formed at 930 °C (a, c) and 970 °C (b, d)

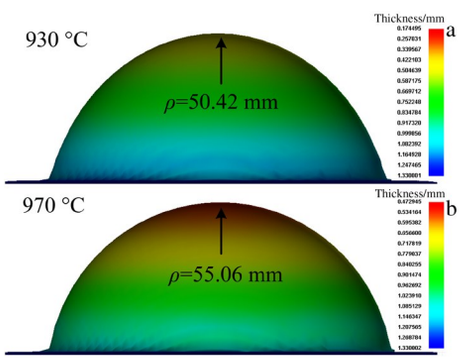

Fig.10 Simulated final bulging parts at 930 °C (a) and 970 °C (b) with h_d=49.85 mm

that the strain rate hardening effect dominates the deformation uniformity of Ti-22Al-25Nb alloy at high temperature, rather than the strain hardening effect. Thus, the smaller strain rate sensitivity at 930 °C leads to the inhomogeneous bulging deformation, and thus the bulging shell evolves into the ellipsoid surface at the top region.

3.3 Wall thickness distribution of bulging part

Fig. 11 shows the theoretical, simulated, and experimental thickness distributions of the bulging parts at 930 and 970 °C. It is noted that the experimental bulging thicknesses are different after bulging at 930 and 970 °C, and the theoretical thicknesses are mostly lower than the simulated and experimental ones. This is because the theoretical thickness calculation is based on the assumption that the shell belongs to the spherical part surface, and the effect of mechanical properties of alloy is neglected. In addition, the simulated thickness agrees well with the experimental one at the bottom regions, but their difference is large at the top region. Such deviation at top region may be attributed to the effect of strain rate sensitivity. The strain rate sensitivity m is decreased with increasing the strain rate in Ti-22Al-25Nb alloy during high temperature deformation[28]. The top region of the bulging part is severely deformed during the bulging process. Therefore, the strain rate is higher and the strain rate sensitivity m is lower than those in other regions. However, the strain rate sensitivity is set as constant in the simulation, which results in the deviation of thickness at top region.

Moreover, the thickness distribution is obviously inhomogeneous and the three curves all show the similar decreasing tendency. The wall thickness decreases from the bottom region to top region. The thinning ratio is the highest at the top region: it reaches 65.4% and 71.8% at 930 and 970 °C, respectively. This is attributed to the fact that the strain distribution is inhomogeneous in the bulging part. The flange region does not deform and the shape does not change during bulging, whereas the inside region deforms under the gas pressure and dominates the shape change. The strain on the flange region is along the tangential direction and ND. The top region suffers a bi-directional tensile strain. The thickness distributions under the same bulging height after bulging at 930 and 970 °C are shown in Fig.11c. The bulging height is set as 49.85 mm. The thinning ratio reaches 66.2% and 60.2% at 930 and 970 °C, respectively. The thinning ratio is smaller and the thickness distribution is more homogeneous at 970 °C. This is because the larger m value at 970 °C leads to the homogeneous deformation and uniform thickness distribution[13].

3.4 Microstructure and mechanical properties of bulging part

Fig. 12 shows SEM microstructures at bottom and top regions after bulging at 930 and 970 °C. At 930 °C, a large amount of O phase is precipitated in the B2 matrix, as shown in Fig. 12a and 12b. However, the microstructures are

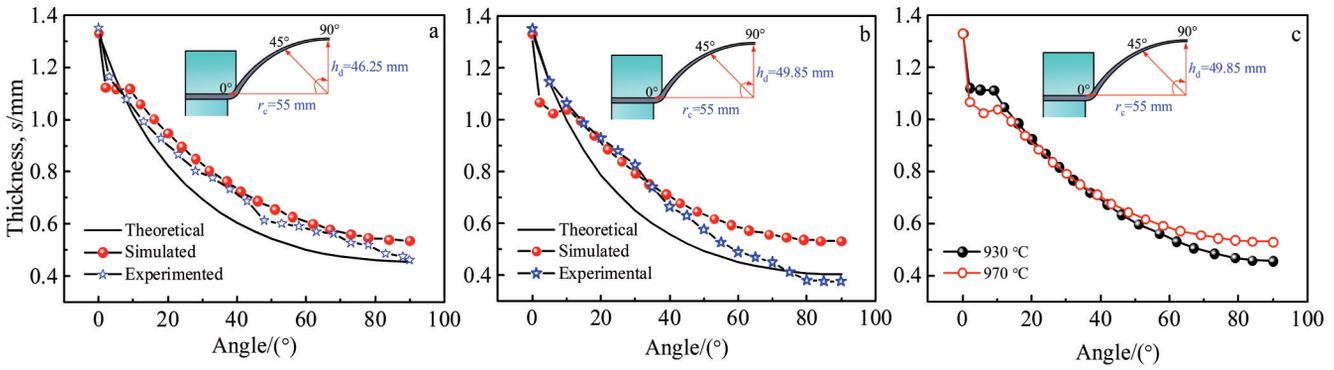

Fig.11 Theoretical, simulated, and experimental thickness distributions of bulging parts formed at 930 °C with h_d=46.25 mm (a) and at 970 °C with h_d=49.85 mm (b); comparison of simulated thickness distributions of bulging parts formed at 930 and 970 °C with h_d=49.85 mm (c)

completely different at bottom and top regions, which indicates the inhomogeneous deformation. The O phase presents the lamellar morphology at the bottom region due to the restricted deformation. At the top region, the O phase is already spheroidized during the bulging process, and the B2 phase is located among the O phase grains. This microstructure is beneficial to the superplastic deformation. At 970 °C, the microstructures at the bottom and top regions are similar, as shown in Fig. 12c and 12d, indicating the homogeneous deformation. The O phase rim also forms outside the equiaxed α_2 grain. In this case, the O phase rim acts as lubricant between different phases, which reduces the tendency of cavity[8,29]. The lamellar O phase is precipitated in the B2 matrix, exerting the strengthening effect on the bulging part[30–31].

The above results all illustrate that the deformation is inhomogeneous during bulging at 930 °C. This may introduce defects in the bulging parts and damage the formability[32]. Generally, the number and size of the defects are large at the top region due to the large deformation degree. As shown in Fig. 13, the V type and O type cavities both exist at the top region of bulging part formed at 930 °C. These cavities are generated during bulging process with O phase precipitation and spheroidization. The V type cavities are located among the adjacent equiaxed O phases, as shown in Fig.13a. Forming V type cavities requires large energy because of their large surface area. Therefore, the V type cavities are usually generated at high strain rates. At high strain rate, the high flow stress leads to the stress concentration and supplies the formation energy. The O type cavities are located at the O(α_2)/B2 phase boundaries, as shown in Fig. 13b. The formation of O type cavities requires low energy, so they can be formed at low strain rates. The V type cavities with high energy are unstable. They may transform to the O type cavities by atom

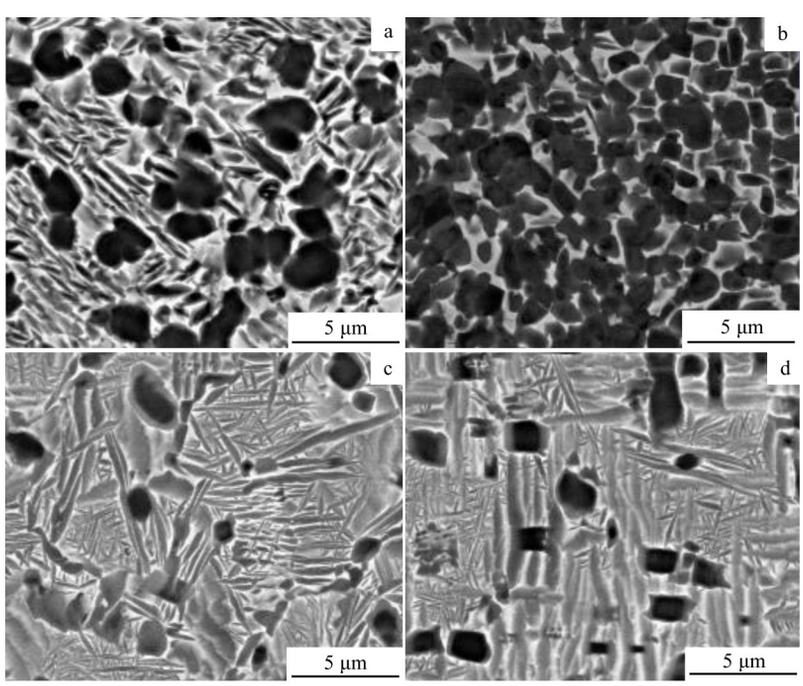

Fig.12 SEM microstructures of bottom (a, c) and top (b, d) regions of bulging parts formed at 930 °C (a, b) and 970 °C (c, d)

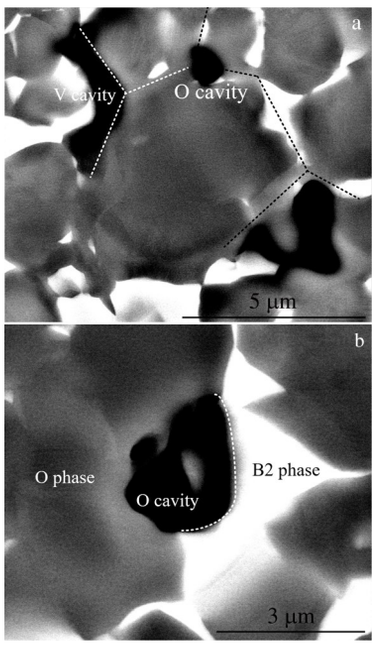

Fig.13 TEM microstructures of cavities at top region of bulging parts formed at 930 °C: (a) V type cavities and (b) O type cavities

diffusion and release partial energy. So, the O type cavities are dominant in the bulging part. Thus, the cavities are generated with O phase precipitation and spheroidization, which causes damage to the formability and mechanical properties of alloys. Therefore, the amount of equiaxed O phase in the bulging part should be strictly restricted to decrease the cavities.

Fig.14 shows the microhardness distributions of the bulging parts formed at 930 and 970 °C. It can be seen that the microhardness is decreased with increasing the deformation degree from the bottom region to the top region. The microhardness on the top region of bulging part formed at 930 °C is lower than that of the original sheet. This is because the precipitated and spheroidized O phase is large, which damages the strength and weakens the solution strengthening effect of Al element[33]. However, the bottom region is hardly

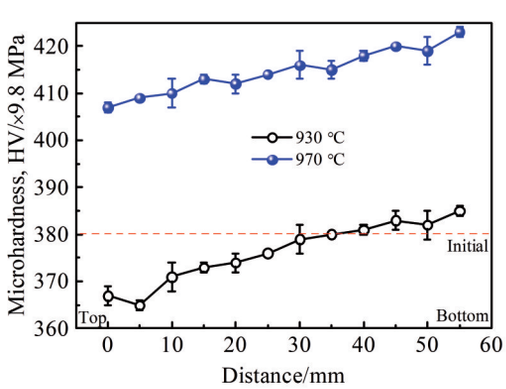

Fig.14 Microhardness distributions of bulging parts formed at 930 and 970 °C

deformed during bulging process. The small lamellar O phase is precipitated at bottom region during the subsequent cooling process, which strengthens the bulging part[30]. At 970 °C, the overall microhardness is higher than that of the original sheet. This is because the small precipitated O phase can strengthen the bulging part. The low microhardness on the top region may be attributed to the recovery effect[32,34]. It is reported that the hot deformation is dominantly controlled by the grain boundary sliding and the dynamic recovery in Ti_2AlNb-based alloys[35]. The recovery at high temperature may release the dislocation accumulation and weaken the strengthening effect. Therefore, the distribution of microstructures and properties is uniform after bulging at 970 °C, and the bulging part is aging-strengthened. Briefly, 970 °C is the optimal deformation temperature for Ti_2AlNb-based alloys.

4 Conclusions

1) During hot gas bulging process, the bulging shell of Ti-22Al-25Nb alloy is close to the spherical surface in the initial bulging stage, and gradually changes to ellipsoid surface with increasing the bulging height. The curvature radius of top region is decreased with increasing the bulging height. The experimental bulging height reaches 46.25 and 49.85 mm and the experimental curvature radius on the shell top reaches 49.33 and 49.19 mm at 930 and 970 °C, respectively. The simulated curvature radius on the shell top reaches 50.42 and 55.06 mm at 930 and 970 °C under the same bulging height of 49.85 mm, respectively. The low bulging temperature causes small curvature radius and leads to the ellipsoid shell surface, which is due to the inhomogeneous bulging deformation with low strain rate sensitivity index *m*.

2) The wall thickness of bulging part is inhomogeneous, which decreases from the bottom region to the top region. The experimental thinning ratio is the highest at the top region of bulging part, which reaches 65.4% and 71.8% at 930 and 970 °C, respectively. However, under the same bulging height of 49.85 mm, the simulated thinning ratio reaches 66.2% and 60.2% at 930 and 970 °C, respectively. The thickness distribution is more homogeneous at 970 °C because the larger *m* value leads to the uniform deformation.

3) The deformation temperature strongly affects the microstructure of bulging part. The O phase is precipitated and spheroidized during bulging process at 930 °C, which causes the generation of O type and V type cavities, thereby decreasing the microhardness. However, the microstructure is distributed uniformly after bulging process at 970 °C. The precipitated O phase has lamellar morphology and can strengthen the bulging part. Therefore, 970 °C is the optimal deformation temperature for Ti_2AlNb-based alloys.

References

1 Banerjee D. *Philosophical Magazine A*[J], 1995, 72(6): 1559
2 Wu Y, Wang D J, Fan R L *et al. Rare Metal Materials and Engineering*[J], 2020, 49(6): 1825
3 Nandy T K, Banerjee D. *Intermetallics*[J], 2000, 8(9–11): 1269

4 Xue Kemin, Hu Yong, Shi Yingbin *et al*. *Rare Metal Materials and Engineering*[J], 2019, 48(8): 2556 (in Chinese)
5 Banerjee D, Gogia A K, Nandi T K *et al. Acta Metallurgica*[J], 1988, 36(4): 871
6 He Yongsheng, Hu Rui, Luo Wenzhong *et al*. *Rare Metal Materials and Engineering*[J], 2018, 47(11): 3460 (in Chinese)
7 Li Yanjun, Zhao Yue, Wu Aiping *et al*. *Rare Metal Materials and Engineering*[J], 2017, 46(5): 1341 (in Chinese)
8 Lin P, He Z B, Yuan S J *et al. Journal of Alloys and Compounds* [J], 2013, 578: 96
9 Lei Z L, Zhang K Z, Zhou H *et al. Journal of Materials Processing Technology*[J], 2018, 255: 477
10 Gogia A K, Nandy T K, Banerjee D *et al. Intermetallics*[J], 1998, 6(7): 741
11 Germann L, Banerjee D, Guédou J Y *et al. Intermetallics*[J], 2005, 13(9): 920
12 Jia J B, Zhang K F, Jiang S S. *Materials Science and Engineering A*[J], 2014, 616: 93
13 Lin P, He Z B, Yuan S J *et al. Materials Science and Engineering A*[J], 2012, 556: 617
14 Wang K H, Liu G, Zhao J *et al. Materials & Design*[J], 2016, 91: 269
15 Gao T J, Wang X, Liu S Q *et al*. *Rare Metal Materials and Engineering*[J], 2020, 49(12): 4010
16 Paul A, Strano M. *Journal of Materials Processing Technology* [J], 2016, 228: 160
17 Liu G, Dang K X, Wang K H *et al. Procedia Manufacturing*[J], 2020, 50: 265
18 Wu Y, Liu G, Liu Z Q *et al. Materials & Design*[J], 2016, 108: 298
19 Kong B B, Liu G, Tao W *et al. Materials Characterization*[J], 2017, 131: 116
20 Wu Y, Liu G, Jin S Y *et al. The International Journal of Advanced Manufacturing Technology*[J], 2017, 92(9): 4583
21 Jiao X Y, Liu Z Q, Wu Y *et al. MATEC Web Conferences*[J], 2018, 190: 7001
22 Song Y Q, Zhao J. *Materials Science and Engineering*[J], 1986, 84: 111
23 Hill R. *The London, Edinburgh, and Dublin Philosophical Magazine and Journal of Science*[J], 1950, 41(322): 1133
24 Zavodov A V, Nochovnaya N A, Lyakhov A A *et al. Materials Characterization*[J], 2021, 180: 111 438
25 Wang S B, Xu W C, Shao B *et al. Journal of Materials Science & Technology*[J], 2022, 101(6): 1
26 Kim H S, Hong S I, Seo M H. *Journal of Materials Research*[J], 2001, 16(3): 856
27 Ghosh A K. *Acta Metallurgica*[J], 1977, 25(12): 1413
28 Lin P, Hao Y G, Zhang B Y *et al. Materials Science and Engineering A*[J], 2018, 710: 336
29 Wu Y, Wang D J, Liu Z Q *et al. International Journal of Mechanical Sciences*[J], 2019, 164: 105 126
30 Zhang K Z, Lei Z L, Chen Y B *et al. Materials Science and Engineering A*[J], 2019, 744: 436
31 Wang G F, Li X, Liu S Y *et al. The International Journal of Advanced Manufacturing Technology*[J], 2018, 99(1): 773
32 Boehlert C J, Majumdar B S, Seetharaman V *et al. Metallurgical and Materials Transactions A*[J], 1999, 30(9): 2305
33 Chen W, Chen Z Y, Wu C C *et al. Intermetallics*[J], 2016, 75: 8
34 Zheng Y P, Zeng W D, Li D *et al. Materials & Design*[J], 2018, 158: 46
35 Li B Y, Zhang K F, Yao W *et al. Materials Characterization*[J], 2019, 150: 38

Ti-22Al-25Nb合金板材气压胀形实验及数值模拟

殷宏亮[1]，孟令健[1]，鲁羽鹏[1]，林　鹏[1,2]
(1. 太原理工大学 材料科学与工程学院，山西 太原 030024)
(2. 哈尔滨工业大学 金属精密热加工国家级重点实验室，黑龙江 哈尔滨 150001)

摘　要：通过气压胀形实验和数值模拟研究了Ti-22Al-25Nb合金板材在高温下的热成形行为，并分析了在930和970 ℃下的胀形球壳形状和壁厚分布，讨论了胀形部分的微观结构和力学性能。结果表明，在胀形初期，胀形球壳接近球面，随胀形高度的增加逐渐椭球化。在930和970 ℃下，最终胀形高度分别达到46.25和49.85 mm，壳顶的曲率半径分别达到49.33和49.19 mm。胀形部分壁厚不均匀，从底部至顶部逐渐减小。变形温度对球壳形状影响较大，在930 ℃时胀形局部形状更加不均。在相同的胀形高度下，930 ℃下的胀形球壳曲率半径较小且壁厚减薄率较高。此外，在930 ℃胀形过程中，O相析出并球化，导致O型、V型空洞的产生且硬度下降。而在970 ℃胀形后，微观组织分布均匀，O相在冷却过程中以层片形式析出，强化了胀形件。

关键词：Ti_2AlNb；气压胀形；热成形性；微观组织

作者简介：殷宏亮，男，1997年生，硕士，太原理工大学材料科学与工程学院，山西 太原 030024，E-mail：13613450080@163.com